# Direct *In Situ* Probe of Electrochemical Processes in Operating Fuel Cells

Stephen S. Nonnenmann,[†] Rainer Kungas,[‡] John Vohs,[‡] and Dawn A. Bonnell[†,*]

[†]Department of Materials Science and Engineering, University of Pennsylvania, LRSM Building/3231 Walnut Street, Philadelphia, Pennsylvania 19104, United States and [‡]Department of Chemical and Biomolecular Engineering, University of Pennsylvania, Towne Building 220 South 33rd Street, Philadelphia, Pennsylvania 19104, United States

ABSTRACT
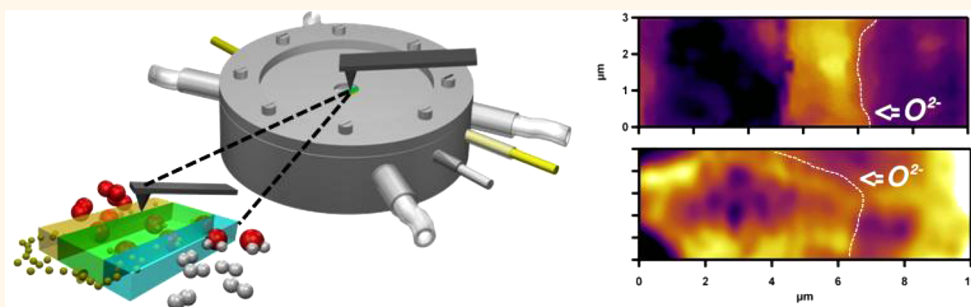
The function of systems and devices in many technologically important applications depends on dynamic processes in complex environments not accessible by structure and property characterization tools. Fuel cells represent an example in which interactions occur under extreme conditions: high pressure, high temperature, in reactive gas environments. Here, scanning surface potential microscopy is used to quantify local potential at electrode/electrolyte interfaces in operating solid oxide fuel cells at 600 °C. Two types of fuel cells are compared to demonstrate two mechanisms of ionic transport at interfaces. Lanthanum strontium ferrite−yttria-stabilized zirconia (LSF-YSZ) and lanthanum strontium manganite−yttria-stabilized zirconia (LSM-YSZ) cross-sectional electrode assemblies were measured to compare mixed ionic electronic conducting and electronic conducting mechanisms. Direct observation of the active zones in these devices yields characteristic length scales and estimates of activation barrier changes.

KEYWORDS: fuel cells · interfaces · scanning probe microscopy · triple phase boundary · cathodes

The most promising strategies for addressing global energy challenges rely on complex materials systems (solar cells, batteries, supercapacitors, and fuel cells) that contain multiple compounds, interfaces, and junctions.[1] Device functionality often involves dynamic electrochemical interactions occurring in extreme environments. Solid oxide fuel cells (SOFCs), for example, comprise a series of several dissimilar materials and phases in contact (cathode/electrolyte/anode)[2−5] and operate at 500−1000 °C in reactive gaseous environments,[6] directly converting chemical energy into electrical energy and heat. The key advantages of SOFCs, that is, high conversion efficiencies,[2] fuel flexibility,[7] and relatively high power output,[8] require high operating temperatures to ensure reaction efficiencies and electrolytic ionic conductivity.[9,10] Here we report on direct, local imaging of electrochemical phenomena occurring at electrode−electrolyte interfaces of operational symmetrical fuel cells using *in situ* scanning probe microscopy. At 600 °C, sharp potential variations indicate interfacial space-charge regions, yielding direct mapping of the active zone and triple phase boundary widths and estimates of activation energy changes. These developments demonstrate the effectiveness of scanning probe techniques in resolving electrochemical phenomena on technologically relevant length scales under realistic operating conditions.

Many of the fundamental processes that underlie the function fuel cells occur at or near interfaces.[2−5] To date, idealized experiments, *ex situ* analysis,[11−13] *operando* spectroscopy,[14,15] and macroscopic electrical property measurements[4−7,16] have driven advancements in SOFCs; however, *in situ* (*operando*) imaging techniques capable of locally resolving the governing
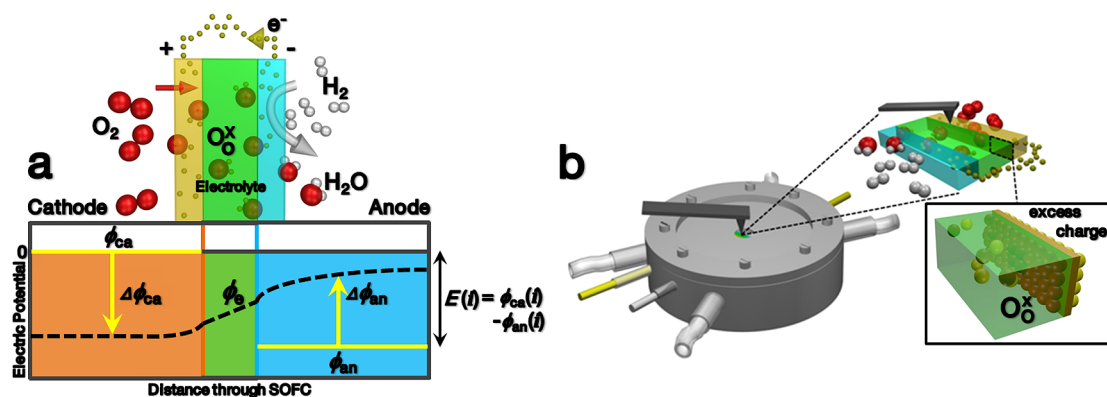
Figure 1. (a) Illustration of SOFC operation under cross section, with the electric potential distribution across the SOFC cross section, under bias. (b) Environmental sample chamber that enables SPM within the operating regime (details in the Supporting Information); the SPM tip probes cell interfaces while under operating conditions; electric double-layer potentials form *via* charge-transfer reactions across the interface.

electrochemical phenomena under realistic operating conditions have remained largely elusive.[17] In particular, direct localized imaging of electrode active zones, triple phase boundaries (TPB), and interfacial electrochemical phenomena under operating conditions have yet to be realized. The scanning probe approach presented here demonstrates, for the first time, direct imaging of local interfacial potential perturbations across electrode–electrolyte interfaces. By comparing fuel cells based on two common electrode materials, we also demonstrate the ability to image and distinguish between bulk-mediated and surface-mediated transport mechanisms, identify both the active zone and triple phase boundary regions, and directly estimate activation barrier changes in these systems.

RESULTS AND DISCUSSION

The length scale associated with the electrochemical processes in fuel cells ranges from 1 nm to 5 μm. Scanning probe microscopy (SPM) is an effective toolbox for characterizing complex properties in this regime,[18] with demonstrated success on oxide compounds[19−22] in ambient conditions. In order to access local properties at high temperatures, we developed an environmental chamber (Figure 1) that allows the spatial resolution of the SPM to be exploited under SOFC operating conditions (600 °C, air atmosphere, $P_{O_2} \sim 0.001$ atm). Figure 1a illustrates SOFC operation and the average and macroscopic electrical potential distribution across the cell,[23] where the difference between the electric potentials of the current collectors (cathode/anode) defines the cell potential. Symmetrical fuel cells comprise identical cathode and anode materials separated by an electrolyte, where an applied lateral bias induces (reversible) cathodic oxygen reduction and anodic oxygen evolution reactions. Within the fuel cell, the electrolyte exhibits Ohmic resistance; electrode potentials ($\phi_{et,ca}$, $\phi_{et,an}$) typically possess different values which arise from the formation of interfacial electric

double-layer potential steps, as defined in an elementary kinetic model:[23]

$$\Delta\phi_{ca}(x) = \phi_{et,ca}(x) - \phi_{elyt,ca}(x)$$
$$\Delta\phi_{an}(x) = \phi_{et,an}(x) - \phi_{elyt,an}(x) \quad (1)$$

where ϕ_{elyt} represents the potential within the electrolyte just beyond the space-charge region of the interface and x represents the distance through the cell.

Strontium (Sr)-doped lanthanum manganite (LSM) is one of the most commonly used perovskite materials for SOFC cathodes, essentially behaving as an electronic conductor, which limits SOFC cathode reactions to TPB regions. In contrast, in SOFC electrodes composed of mixed ionic/electronic conducting (MIEC) electrode materials, such as Sr-doped lanthanum ferrite (LSF) and Sr-doped $LaCo_yFe_{1−y}O_3$ (LSCF), the reaction zone extends from the TPB into the electrode bulk. Therefore, using tape-casted electrolytes and powder-ink printed electrodes, we fabricated two symmetrical fuel cell types: LSF–yttria-stabilized zirconia (YSZ) and LSM–YSZ assemblies to enable direct comparison between the electrochemical processes of electronic conducting and MIEC electrode materials. Materials characterization, including X-ray diffraction and macroscopic impedance measurements, can be found elsewhere.[24,25] Electrodes prepared using this process typically have a particle size on the order of 0.2 μm in diameter with a porosity of approximately 25% (see Supporting Information).[26] Dense YSZ electrolytes prepared using this method are polycrystalline in nature, with an average grain size between 6 and 8 μm.[27] The chamber geometry permits cross-sectional cell characterization, accessing the potential gradients occurring within the electrodes and electrolytes (see Supporting Information).

To demonstrate direct observation of charge-transfer reactions and double-layer formation, we employed scanning surface potential microscopy (SSPM) (also called Kelvin force microscopy) to map local potential variations on cross-sectional surfaces (Figure 2). For the
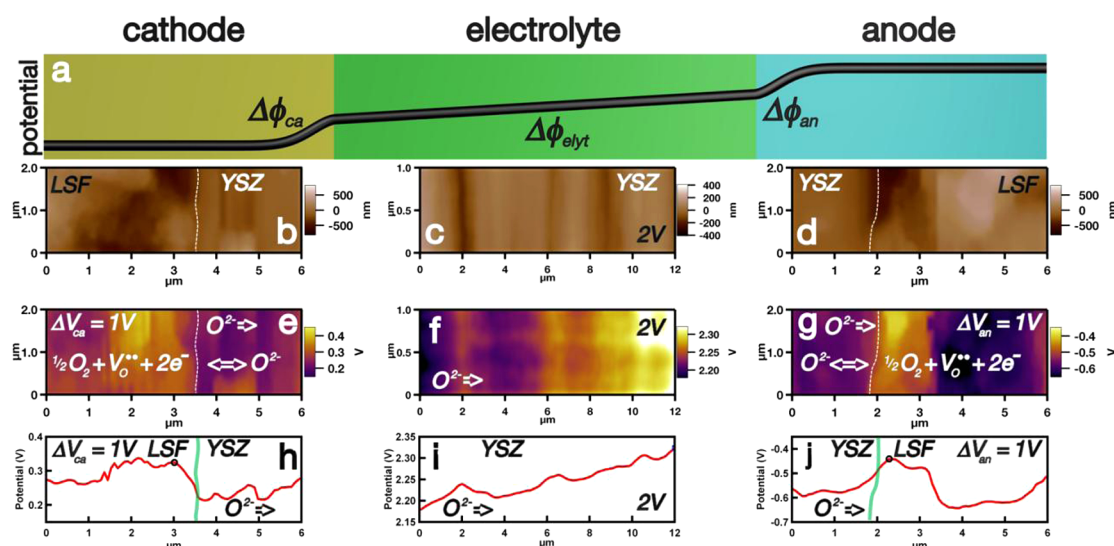
Figure 2. (a) Schematic of potential distribution (black) across the effective cathode (orange), electrolyte (green), and effective anode (blue); topographic (b−d) and scanning surface potential (e−g) images of a biased symmetrical LSF-YSZ SOFC collected at 600 °C, showing (from left) the effective cathode−electrolyte interface (b,e; white dotted line, $\Delta 1\ V_{an}$ applied anodically), YSZ electrolyte (c,f; 2 V applied bias), and effective anode−electrolyte interface (d,g; white dotted line, $\Delta 1\ V_{ca}$ applied cathodically); oxygen ion direction and reduction/evolution reactions are indicated at the interface; (h−) profiles averaged over 15 lines; the light green lines in (h,j) represent the interfaces. $V_O^{\bullet\bullet}$ and O^{2-} represent an oxygen vacancy and oxygen ion, respectively.

mixed ionic electronic conductor electrode LSF-YSZ symmetrical cell, the half-cell reaction takes the form

$$1/2 O_2 + V_O^{\bullet\bullet} + 2e^- \Leftrightarrow O_O^X \qquad (2)$$
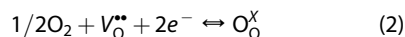
where $V_O^{\bullet\bullet}$ and O_O^X represent an oxygen vacancy and oxygen ion, respectively.

An operational fuel cell should display the potential profiles shown in Figure 2a. The topographic images are shown for the cathode/electrolyte (Figure 2b), YSZ electrolyte (Figure 2c), and anode/electrolyte (Figure 2d) regions. The surface potential images (Figure 2e−g) and line profiles (Figure 2h−j) of a symmetrical LSF-YSZ fuel cell collected at 600 °C clearly indicate that the SOFC is operating. The dotted white lines represent the electrode/electrolyte interface (Figure 2b,e cathode; 2d,g anode), determined through clear topographic structural differences between the LSF electrode and the YSZ electrolyte (Figure 2b,d). Charge transfer within the LSF-YSZ electrode starts with the adsorption of molecular oxygen on a perovskite lattice vacancy site $V_O^{\bullet\bullet}$ followed by dissociation into O_O^X and incorporation into the electrolyte.[28,29] Line profile analysis (Figure 2h−j) provides a more detailed assessment of the interface and SOFC operational behavior. Significantly, the potential variations appear nearly identical to those shown in Figures 1b and 2a. Local potential variations occur within the cathode (Figure 2b) near the interface (light green line), where a small, sharp drop occurs (between the green line and black circle). The potential displays near Ohmic behavior as it extends toward the interface and into the electrolyte (Figure 2c,f,i). The surface potential within the YSZ electrolyte displays

a linear-like profile (Figure 2i), with small variations occurring due to local topographic features such as grain boundaries. These small features however only deviate 0.7% on average from a linear fit of the slope (Supporting Information). Adjacent to the anode interface (Figure 2g), the local resistance changes from near-Ohmic character within the electrolyte region to a perturbation after the interface (Figure 2j, green line to black circle) and into the electrode. Since oxygen vacancies are charged defects, a spatial variation in vacancy concentration results in variations in potential measured with SPM. The potential of both electrodes immediately adjacent to the interface with the electrolyte is higher than that some distance from the interface. At the cathode, oxygen transfer to the electrolyte is expected to be rate-limiting, leading to an increase in oxygen locally and an associated decrease in vacancy concentration. At the anode, oxygen enters the electrode lattice filling in vacancies, again producing a local decrease in oxygen vacancy concentration with respect to that of the bulk electrode. Similarly, the oxygen vacancy concentration gradient in the electrolyte is reflected in the potential gradient.

Considering the portion of the electrode areas of highest potential (Figure 2h, left, and Figure 2j, right), we estimate that the extended active region observed here for the LSF-YSZ system is approximately between 1.4 and 2.1 μm, in reasonable agreement with studies of similar systems.[30] The localized cathodic (102 mV, Figure 2h) and anodic (60 mV, Figure 2j) double-layer potential variations, and measured operating current density of 133 mA/cm^2, yields a double-layer resistance of 6−10 Ω cm^2 which is within the range of
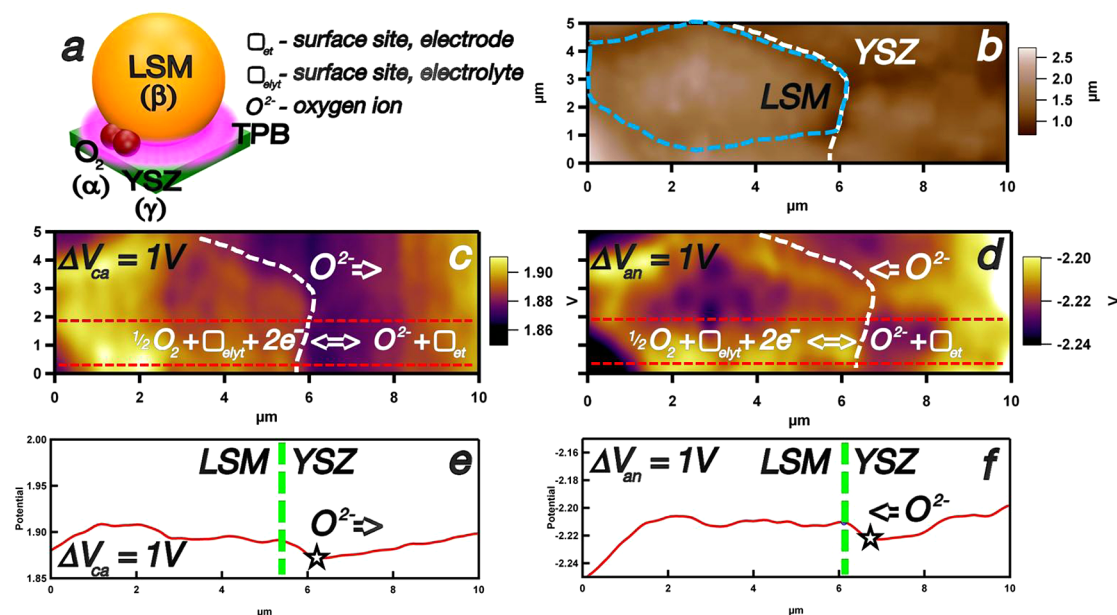
Figure 3. (a) Illustration of TPB formation at the LSM-YSZ interface; topographic (b) and scanning surface potential (c,d) images of a biased symmetrical LSM-YSZ SOFC collected at 600 °C, shown with effective cathode−electrolyte interface (c, white dotted line, $\Delta 1\,V_{ca}$ applied cathodically) and effective anode−electrolyte interface (d, white dotted line, $\Delta 1\,V_{an}$ applied anodically). Oxygen ion direction and reduction/evolution reactions are indicated at the interface. (e,f) Profiles averaged over 20 lines between the red dotted lines (c,d) of the local potential; the green dotted lines represent the interfaces.

expected values for temperature.[31] The associated change to the activation barrier from equilibrium ΔG_R to produce a net current for the forward barrier case is expressed as[32]

$$\Delta G_R = \alpha z F \eta_{act} \qquad (3)$$

where α is the charge-transfer coefficient (typically $\alpha = 0.5$), z the number of redox equivalents within the reaction ($z = 2$), F is Faraday's constant, and η_{act} the activation potential. The stated assumptions for α and z and the measured values for activation potential yield ΔG_R values between 6 and 10 kJ/mol, in reasonable agreement with recent results for activating surface exchange in a similar mixed conducting oxide, LSCF.[33]

We examined electrically conducting LSM electrode interfaces to determine differences between cells exhibiting bulk-dominated and surface-dominated processes (Figure 3). LSM-based symmetrical cells rely on surface-mediated charge transfer occurring along the TPB (Figure 3a), in contrast to the bulk-mediated processes observed in Figure 2. Figure 3 shows topographic (Figure 3b) and surface potential (Figure 3c,d) images of an LSM-YSZ interface (white dotted line). Here the LSM grain closest to the interface (Figure 3b, light blue dotted line) displays electrical potential inhomogeneity (Figure 3c,d), with increased potential observed at the grain boundaries closest to the TPB and potential minima occurring within the grain bulk.

This behavior is consistent with the expected surface-mediated processes that govern TPB formation within LSM-based systems.[4,5] Given the inherently low

$[V_O^{\bullet\bullet}]$ of LSM, the predominant charge-transfer mechanism relies on surface oxygen vacancy migration to the adsorbed molecules, where dissociation occurs without a barrier, and a rate-determining step involves the incorporation of ionic species into the electrolyte:[23,24]

$$1/2O_2 + \square_{elyt} + 2e_{et}^- \leftrightarrow O_O^X + \square_{et} \qquad (4)$$
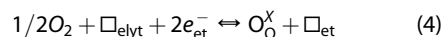
where $\square$ is a free surface site and "elyt" and "et" denote electrolyte and electrode, respectively. Line profile analyses show localized, linear interfacial resistance variations between the dotted green lines and star markers (Figure 3e,f). The measured drop at the cathode interface (18 mV) is larger than that of the anode interface (11 mV), and occurs over a larger distance (860 nm, cathode; 470 nm, anode); significantly, these agree reasonably with recent studies.[29] The higher activation potential of the cathode side suggests a larger barrier at the interface, consistent with the mechanism involving incorporation of the ionic species into the electrolyte.[23] The charge transfer is expected to occur around the TPB, considered to be the area of highest potential occurring at the interface (Figure 3e,f) or the overlapping region between the dotted white line and dotted blue line in the topographic image (Figure 3d), estimated here to be 1.6 μm in length. Using eq 3, we estimate ΔG_R between 1 and 2 kJ/mol for LSM.

Two issues arise in considering how quantitatively SPM relates to the properties at real interfaces. The first concerns the contribution of measurement errors in surface potential acquisition; the second relates to the fact that the interfaces are exposed rather than in the

bulk. In SSPM, the sum of the surface potential and contact potential difference is probed. As with all electrostatic and electrodynamic scanning probes (EFM, SIM, etc.), SSPM is susceptible to parasitic capacitance from the cantilever and tip cone.[34−36] In addition, nonlinear feedback control errors are dependent on applied voltage[37] and can play a role for topographically rough surfaces.[38−40] These are commonly referred to as cross-talk errors. Using frequency modulation rather than amplitude modulation and operating with voltage modulations <5 V minimizes these errors. More importantly, to the extent that these contributions are constant during the measurement, which holds for constant operating parameters and tip condition, the differences in potential are quantitative. The facts that the linear resistance of the electrolyte over 10 μm from Figure 2 is within 20% of the macroscopic value and that the ΔG_R for the electrode/YSZ interface is within an order of magnitude of that for bulk together indicate that the measured potential differences are accurate to within 15−25%. The cross-sectional configuration of this approach enables direct access to the relevant interfaces in the fuel cell but raises the question of possible deviation of surface properties from bulk behavior. In operating in ambient conditions, it is possible for molecular adsorption to influence the results. Indeed, we have shown that in the case of ferroelectric surfaces (which is extreme in that polarization encourages adsorption), molecular adsorption systematically affects surface potential.[41] However, on most oxides, environmental adsorbates desorb at low temperatures relative to those in fuel cell operation[42] and, therefore, should not play a significant role in our results. In order to avoid possible complications associated with chemical and/or defect concentrations near the surface, the measurements were made under less severe conditions than those used during fuel cell fabrication. During fabrication, samples were equilibrated at 900 °C in ambient oxygen partial pressure for 4 h. In operation, cells were driven with an applied voltage so they were not subject to extrinsic chemical gradients. Therefore, the local properties at the cross-sectional surface should approximate those at the internal interface. The extent to which this varies in more complex chemical environments could be determined with cross-sectional time-dependent analysis.

Finally, while the spatial resolution demonstrated here was ∼100 nm, we predict that 10−25 nm resolution will be achieved in the future. Additionally, it should be noted that we expect the fabrication process to have an effect on the potential profile. The symmetrical cells implemented in this study were of technologically relevant materials and processes, resulting in a porous electrode microstructure. The expectation is that cells grown with dense electrodes to form more intimate interfaces or those grown with infiltrated electrode microstructures[29] would exhibit different potential landscapes.

CONCLUSION

Using SPM imaging at realistic temperatures, we have demonstrated direct, *in situ* observation of localized, interfacial potential variations occurring within an operational fuel cell, for both bulk-mediated and surface-mediated charge-transfer systems. We also demonstrated the effects of polarization activation through estimates of activation barrier changes using the directly measured values of interfacial potential variations and characteristic lengths under realistic operating conditions. The ability to directly correlate electrochemical processes to local topography with nanometer precision offers a path to closing the gap between theoretical prediction/design and macroscopic impedance studies.

METHODS

Experimental. *LSM and LSF Symmetrical Fuel Cell Cross-Sectional Sample Preparation.* Symmetrical fuel cell samples were fabricated using a paste prepared by combining 0.25 g of La$_{0.8}$Sr$_{0.2}$FeO$_{3−\delta}$ (LSF) or La$_{0.8}$Sr$_{0.2}$MnO$_{3−\delta}$ (LSM) powder with 0.04 mL of α-terpineol, which was directly applied to a disk of dense YSZ electrolyte. The LSF and LSM powders were prepared using the Pechini method. For the preparation of LSF, La(NO$_3$)$_3$·6H$_2$O (Alfa Aesar, 99.9%), Sr(NO$_3$)$_2$ (Alfa Aesar, 99%), and Fe(NO$_3$)$_3$·6H$_2$O (Fisher Scientific 98.4%) at a molar ratio of La/Sr/Fe = 0.8:0.2:1 were dissolved in deionized water. Citric acid, in a 1:1 ratio with the metal cations, was added to the aqueous nitrate solution as a complexing agent. The solution was then heated on a hot plate until most of the water had evaporated and a thick paste remained. The mixture was transferred into a crucible and calcined at 1000 °C for 4 h to form the perovskite phase. The preparation of LSM powder was identical, except a Mn precursor (Mn(NO$_3$)$_2$·xH$_2$O, Alfa Aesar, 99.98%) was used instead of Fe(NO$_3$)$_3$·6H$_2$O. The value of x was determined by thermogravimetric measurements and the amount of Mn precursor in the solution adjusted accordingly. The dense YSZ electrolyte disk was prepared by tape-casting a slurry consisting of 80 g of 8 mol % YSZ (TZ8Y, Tosoh), 1.6 g of Menhaden fish oil (R.E. Mistler, Inc.), 7.6 g of polyvinyl butyral based binder (B98, Solutia, Inc.), 2 mL of poly(ethylene glycol) (PEG, Alfa Aesar), 2 mL of benzyl butyl phthalate (BBP, Aldrich), 20 g of xylenes (Sigma-Aldrich), and 40 g of ethanol using a R.E. Mistler tabletop tape-casting system. The green tape was cut into circular pieces of 3/4 in. in diameter and then subjected to constrained sintered at 1500 °C for 4 h. The final YSZ disks had a diameter of 13 mm and thickness of ∼70 μm. After the perovskite paste was applied onto both sides of the YSZ disk, the sample was heated to 800 °C for 4 h to remove organics and to ensure contact with the electrolyte. To ensure proper current collection, each side received a coating of conductive silver paste (SPI supplies, 05063-AB Silver Paste Plus). Samples were then cut by a diamond saw, mounted onto a cross-sectional polishing mount with wax, and polished flat using an Allied polisher.

Environmental Sample Chamber and Calibration. The environmental sample chamber was fabricated of 316 stainless steel with various gaseous, thermal, and electrical feedthroughs and a top access port for integration with an existing, commercially available SPM system. To achieve the temperature range benchmark between 500 and 600 °C to induce the various

electrochemical phenomena, the heating element was calibrated using two thermocouples; the internal chamber thermocouple to provide feedback on the applied thermal load and an external thermocouple placed in direct contact with the edge surface of the sample to record the sample temperature.

Scanning Surface Potential Microscopy. Samples were heated to 600 °C under an applied thermal load of 850 °C using the environmental chamber (details in the Supporting Information). Using a commercial AFM (Asylum Research MFP-3D), this two-pass technique first collected a topographic image of the sample surface in noncontact mode. A second pass was then performed with a conductive tip (Rocky Mountain Nanotech 25Pt400B, f = 12 kHz) under an ac bias (3 V_{ac}) using a lock-in amplifier to detect longer range electrostatic forces between the tip and sample. A feedback loop then applied a dc bias to compensate the contact potential difference between the tip and sample surface which governs the electrostatic force, creating an image of the surface potential of the sample. Scans were first collected of 15 μm × 15 μm (LSF) and 20 μm × 20 μm (LSM) areas, for a total of 256 lines, at a rate of 0.6 Hz.

Conflict of Interest: The authors declare no competing financial interest.

Supporting Information Available: Additional material includes digital photographs and schematic illustrations of the miniature chamber; larger area topographic and surface potential images of the electrode/electrolyte interface; and linear fitting of surface potential within the YSZ electrolyte. This material is available free of charge *via* the Internet at http://pubs.acs.org.

REFERENCES AND NOTES

1. Arićo, A. S.; Bruce, P.; Scrosati, B.; Tarascon, J. M. Nanostructured Materials for Advanced Energy Conversion and Storage Devices. *Nat. Mater.* **2005**, *4*, 366–377.
2. Atkinson, A.; Barnett, S.; Gorte, R. J.; Irvine, J. T. S.; McEvoy, A. J.; Mogensen, M.; Singhal, S. C.; Vohs, J. M. Advanced Anodes for High-Temperature Fuel Cells. *Nat. Mater.* **2004**, *3*, 17–27.
3. Suntivich, J.; Gasteiger, H. A.; Yabuuchi, N.; Nakanishi, H.; Goodenough, J. B.; Shao-Horn, Y. Design Principles for Oxygen-Reduction Activity on Perovskite Oxide Catalysts for Fuel Cells and Metal-Air Batteries. *Nat. Chem.* **2011**, *3*, 546–550.
4. Flieg, J. Solid Oxide Fuel Cell Cathodes: Polarization Mechanisms and Modeling of the Electrochemical Performance. *Annu. Rev. Mater. Res.* **2003**, *33*, 361–382.
5. Adler, S. B. Factors Governing Oxygen Reduction in Solid Oxide Fuel Cell Cathodes. *Chem. Rev.* **2004**, *104*, 4791–4843.
6. Wachsman, E. D.; Lee, K. T. Lowering the Temperature of Solid Oxide Fuel Cells. *Science* **2011**, *334*, 935–939.
7. Park, S.; Vohs, J. M.; Gorte, R. J. Direct Oxidation of Hydrocarbons in a Solid-Oxide Fuel Cell. *Nature* **2000**, *404*, 265–267.
8. Shao, Z.; Haile, S. M.; Ahn, J.; Ronney, P. D.; Zhan, Z.; Barnett, S. A. A Thermally Self-Sustained Micro Solid-Oxide Fuel-Cell Stack with High Power Density. *Nature* **2005**, *435*, 795–798.
9. Beckel, D.; Bieberle-Hütter, A.; Harvey, A.; Infortuna, A.; Muecke, U. P.; Prestat, M.; Rupp, J. L. M.; Gauckler, L. J. Thin Films for Micro Solid Oxide Fuel Cells. *J. Power Sources* **2007**, *173*, 325–345.
10. Garcia-Barriocanal, J.; Rivera-Calzada, A.; Varela, M.; Sefrioui, Z.; Iborra, E.; Leon, C.; Pennycook, S. J.; Santamaria, J. Colossal Ionic Conductivity at Interfaces of Epitaxial ZrO_2:Y_2O_3/$SrTiO_3$ Heterostructures. *Science* **2008**, *321*, 676–680.
11. Wilson, J. R.; Duong, A. T.; Gameiro, M.; Chen, H.-Y.; Thornton, K.; Mumm, D. R.; Barnett, S. A. Quantitative Three-Dimensional Microstructure of a Solid Oxide Fuel Cell Cathode. *Electrochem. Commun.* **2009**, *11*, 1052–1056.
12. Wachsman, E. D. Deconvolution of SOFC Cathode Polarization. *ECS Trans.* **2007**, *7*, 1051–1054.
13. Wilson, J. R.; Kobsiriphat, W.; Mendoza, R.; Chen, H.-Y.; Hiller, J. M.; Miller, D. J.; Thornton, K.; Voorhees, P. W.; Adler, S. B.; Barnett, S. A. Three Dimensional Reconstruction of a Solid-Oxide Fuel-Cell Anode. *Nat. Mater.* **2006**, *5*, 541–544.
14. Zhang, C.; Grass, M. E.; McDaniel, A. H.; DeCaluwe, S. C.; El Gabaly, F.; Liu, Z.; McCarty, K. F.; Farrow, R. L.; Linne, M. A.; Hussain, Z.; *et al.* Measuring Fundamental Properties in Operating Solid Oxide Electrochemical Cells by Using *In Situ* X-ray Photoelectron Spectroscopy. *Nat. Mater.* **2010**, *9*, 944–949.
15. Pomfret, M. B.; Owrutsky, J. C.; Walker, R. A. *In-Situ* Optical Studies of Solid Oxide Fuel Cells. *Annu. Rev. Anal. Chem.* **2010**, *3*, 151–174.
16. Shao, Z.; Haile, S. M. A High-Performance Cathode for the Next Generation of Solid-Oxide Fuel Cells. *Nature* **2004**, *431*, 170–173.
17. Tao, F.; Salmeron, M. *In-Situ* Study of Chemistry and Structure of Materials in Reactive Environments. *Science* **2011**, *331*, 171–174.
18. Bonnell, D. A.; Basov, D. N.; Bode, M.; Diebold, U.; Kalinin, S. V.; Madhavan, V.; Novotny, L.; Salmeron, M.; Schwarz, U. D.; Weiss, P. S. Imaging Physical Phenomena with Local Probes: From Electrons to Photons. *Rev. Mod. Phys.* **2012**, *84*, 1343–1381.
19. Kalinin, S. V.; Shao, R.; Bonnell, D. A. Local Phenomena in Oxides by Advanced Scanning Probe Microscopy. *J. Am. Ceram. Soc.* **2005**, *88*, 1077–1098.
20. Balke, N.; Jesse, S.; Morozovska, A. N.; Eliseev, E.; Chung, D. W.; Kim, Y.; Adamczyk, L.; Garcia, R. E.; Dudney, N.; Kalinin, S. V. Nanoscale Mapping of Ion Diffusion in a Lithium-Ion Battery Cathode. *Nat. Nanotechnol.* **2010**, *5*, 749.
21. Kumar, A.; Ciucci, F.; Morozovska, A. N.; Kalinin, S. V.; Jesse, S. Measuring Oxygen Reduction/Evolution Reactions on the Nanoscale. *Nat. Chem.* **2011**, *3*, 707–713.
22. Kuru, Y.; Jalili, H.; Cai, Z.; Yildiz, B.; Tuller, H. Direct Probing of Nanodimensioned Oxide Multilayers with the Aid of Focused Ion Beam Milling. *Adv. Mater.* **2011**, *23*, 4543–4548.
23. Bessler, W. G.; Gewies, S.; Vogler, M. A New Framework for Physically Based Modeling of Solid Oxide Fuel Cells. *Electrochim. Acta* **2007**, *53*, 1782–1800.
24. McIntosh, S.; Adler, S. B.; Vohs, J. M.; Gorte, R. J. The Effect of Polarization on and Implications for Characterization of LSM-YSZ Composite Cathodes. *Electrochem. Solid State* **2004**, *7*, A111–A114.
25. Huang, Y.; Vohs, J. M.; Gorte, R. J. Fabrication of Sr-Doped $LaFeO_3$ YSZ Composite Cathodes. *J. Electrochem. Soc.* **2004**, *151*, A646–A651.
26. He, H.; Huang, Y.; Regal, J.; Boaro, M.; Vohs, J. M.; Gorte, R. J. Low-Temperature Fabrication of Oxide Composites for Solid-Oxide Fuel Cells. *J. Am. Ceram. Soc.* **2004**, *87*, 331–336.
27. Helmick, L.; Dillon, S. J.; Gerdes, K.; Gemmen, R.; Rohrer, G. S.; Seetharaman, S.; Salvador, P. A. Crystallographic Characteristics of Grain Boundaries in Dense Yttria-Stabilized Zirconia. *Int. J. Appl. Ceram. Technol.* **2011**, *8*, 1218–1228.
28. Wang, L.; Merkle, R.; Mastrikov, Y. A.; Kotomin, E. A.; Maier, J. Oxygen Exchange Kinetics on Solid Oxide Fuel Cell Cathode Materials—General Trends and Their Mechanistic Interpretation. *J. Mater. Res.* **2012**, *27*, 2000–2008.
29. Küngas, R.; Bidrawn, F.; Mahmoud, E.; Vohs, J. M.; Gorte, R. J. Evidence of Surface-Reaction Rate Limitations in SOFC Composite Cathodes. *Solid State Ionics* **2012**, *225*, 146–150.
30. Bidrawn, F.; Küngas, R.; Vohs, J. M.; Gorte, R. J. Modeling Impedance Response of SOFC Cathodes Prepared by Infiltration. *J. Electrochem. Soc.* **2011**, *158*, B514–B525.
31. Niu, Y.; Zhou, W.; Sunarso, J.; Ge, L.; Zhu, Z.; Shao, Z. High Performance Cobalt-Free Perovskite Cathode for

Intermediate Temperature Solid Oxide Fuel Cells. *J. Mater. Chem.* **2010**, *20*, 9619–9622.

32. O'Hayre, R.; Cha, S. W.; Colella, W.; Prinz, F. B. *Fuel Cell Fundamentals*; Wiley: New York, 2006.

33. Armstrong, E. N.; Duncan, K. L.; Oh, D. J.; Weaver, J. F.; Wachsman, E. D. Determination of Surface Exchange Coefficients of LSM, LSCF, YSZ, GDC Constituent Materials in Composite SOFC Cathodes. *J. Electrochem. Soc.* **2011**, *158*, B492–499.

34. Huey, B. D.; Bonnell, D. A. Nanoscale Variation in Electric Potential at Oxide Bicrystal and Polycrystal Interfaces. *Solid State Ionics* **2000**, *131*, 51–60.

35. Kathan-Galipeau, K.; Nanayakkara, S.; O'Brian, P. A.; Nikiforov, M.; Discher, B. M.; Bonnell, D. A. Direct Probe of Molecular Polarization in *De Novo* Protein−Electrode Interfaces. *ACS Nano* **2011**, *5*, 4835–4842.

36. Pingree, L. S. C.; Fabbroni Martin, E.; Shull, K. R.; Hersam, M. C. Nanoscale Impedance Microscopy—A Characterization Tool for Nanoelectronic Devices and Circuits. *IEEE Trans. Nanotechnol.* **2005**, *4*, 255–259.

37. Wu, Y.; Shannon, M. A. AC Driving Amplitude Dependent Systematic Error in Scanning Kelvin Probe Microscope Measurements: Detection and Correction. *Rev. Sci. Instrum.* **2006**, *77*, 043711–9.

38. Ziegler, D.; Stemmer, A. Force Gradient Sensitive Detection in Lift-Mode Kelvin Probe Force Microscopy. *Nanotechnology* **2011**, *22*, 075501.

39. Strassburg, E.; Boag, A.; Rosenwaks, Y. Reconstruction of Electrostatic Force Microscopy Images. *Rev. Sci. Instrum.* **2005**, *76*, 083705–5.

40. Charrier, D. S. H.; Kemerink, M.; Smalbrugge, B. E.; de Vries, T.; Janssen, R. A. Real *versus* Measured Surface Potentials in Scanning Kelvin Probe Microscopy. *ACS Nano* **2008**, *2*, 622–626.

41. Li, D.; Zhao, M. H.; Garra, J.; Kolpak, A. M.; Rappe, A. M.; Bonnell, D. A.; Vohs, J. M. Direct *In Situ* Determination of the Polarization Dependence of Physisorption on Ferroelectric Surfaces. *Nat. Mater.* **2008**, *7*, 473–477.

42. Kalinin, S. V.; Bonnell, D. A. Temperature Dependence of Polarization and Charge Dynamics on the $BaTiO_3(100)$ Surface by Scanning Probe Microscopy. *Appl. Phys. Lett.* **2001**, *78*, 1116–1118.